Direct bulk-sensitive probe of 5*f* symmetry in URu_2Si_2

Martin Sundermann[a], Maurits W. Haverkort[b,1], Stefano Agrestini[b], Ali Al-Zein[c,2], Marco Moretti Sala[c], Yingkai Huang[d], Mark Golden[d], Anne de Visser[d], Peter Thalmeier[b], Liu Hao Tjeng[b], and Andrea Severing[a,3]

[a]Institute of Physics II, University of Cologne, 50937 Cologne, Germany; [b]Max-Planck-Institute for Chemical Physics of Solids, 01187 Dresden, Germany; [c]European Synchrotron Radiation Facility, 38043 Grenoble Cédex, France; and [d]Van der Waals-Zeeman Institute, University of Amsterdam, 1098 XH Amsterdam, The Netherlands

Edited by Zachary Fisk, University of California, Irvine, CA, and approved October 17, 2016 (received for review August 2, 2016)

The second-order phase transition into a hidden order phase in URu_2Si_2 goes along with an order parameter that is still a mystery, despite 30 years of research. However, it is understood that the symmetry of the order parameter must be related to the symmetry of the low-lying local electronic *f*-states. Here, we present results of a spectroscopic technique, namely core-level nonresonant inelastic X-ray scattering (NIXS). This method allows for the measurement of local high-multipole excitations and is bulk-sensitive. The observed anisotropy of the scattering function unambiguously shows that the 5*f* ground-state wave function is composed mainly of the Γ_1 with majority $J_z = |4\rangle + |-4\rangle$ and/or Γ_2 singlet states. The incomplete dichroism indicates the possibility that quantum states of other irreducible representation are mixed into the ground state.

strongly correlated electron systems | X-ray spectroscopy | crystal-electric field | heavy fermions | hidden order

In heavy fermion rare earth or actinide compounds, the f electrons are well localized at high temperatures, but as temperature is lowered, hybridization with conduction electrons becomes increasingly effective, resulting in a more itinerant f-electron character at low temperatures. These hybridized f electrons form narrow bands and have large effective masses. Quasiparticle interaction effects in these narrow bands are responsible for the many exciting phenomena present in heavy fermion compounds: multipolar order (1), unconventional superconductivity (2), or quantum criticality (3). The hidden order phase in URu_2Si_2 is one example of the exotic low-temperature phases found in this material class. URu_2Si_2 is a tetragonal heavy fermion compound that undergoes two phase transitions, the nonmagnetic hidden order (HO) transition at $T_{HO} = 17.5$ K, which involves an appreciable loss of entropy, and a superconducting transition at about 1.5 K (4–7). Below the HO transition, small-ordered magnetic moments were observed in the earlier studies but were determined later to belong to a parasitic minority phase. With applied pressure ($p \geq 0.7$ GPa), the HO order is replaced by an antiferromagnetic phase with large-ordered moments (so-called $LMAF$-phase) (8). The order parameter of the HO phase has been the subject of intense investigations for more than 30 years but, so far, has remained hidden, which has been the inspiration for its name. This second-order transition into an electronically ordered state involves a reconstruction of the Fermi surface (9, 10) and a change of quasiparticle scattering rate (11). The Fermi surfaces of the HO and high-pressure $LMAF$ phase are very similar (12).

In URu_2Si_2 three-energy scales have been identified: a hybridization gap of $\Delta_{hyb} \approx 13$ meV [150 K] (13) that opens below 27 K, another gap that opens in the HO phase with $\Delta_{HO} \approx 4.1$ meV [50 K] in the charge (9, 10, 14, 15) as well as spin channel (16, 17), and a resonance mode that appears in the HO gap at $\cong$1.6 meV [18 K], also in both channels (18–20). Furthermore, with entering the HO phase, the breaking of the fourfold rotational symmetry has been reported from torque experiments (21), high resolution X-ray diffraction on high quality crystals (22), and elastoresistance measurements (23). For a more detailed experimental and theoretical survey of physical properties of URu_2Si_2, we refer to the review article by Mydosh and Oppeneer (24).

In intermetallic actinide compounds, the valence state is often intermediate, and indeed, N-edge sum rules (25), lifetime reduced L-edge absorption (26), and soft X-ray photoelectron spectroscopy measurements (27) find a valence between 3^+ and 4^+ for URu_2Si_2. URu_2Si_2 is an itinerant system, and yet electron correlations on the U atom will reduce the charge fluctuations and favor also a particular local irreducible representation (28). In this respect, it is suggestive to assume that the U^{4+} f^2 configuration will give the dominant contribution, which is in line with first-principle dynamical mean-field theory (DMFT) calculations (29). The question is now which of the U^{4+} (f^2) states build up the itinerant state and lead to the formation of the HO. The present work presents the asymmetry of the inelastic X-ray scattering function $S(\vec{q},\omega)$, as measured in a bulk-sensitive, nonresonant inelastic X-ray scattering (NIXS) experiment, and gives direct and quantitative information on the 5f symmetry in URu_2Si_2.

To address the local 5f degrees of freedom of URu_2Si_2, we will make use of the crystal-electric field (CEF) description of the U^{4+} f^2 configuration in D_{4h} symmetry. The CEF splits the ninefold degenerate $J = 4$ multiplet into five singlets and two doublets, which can be written in the following way when using the J_z representation:

Significance

The hidden order problem in URu_2Si_2 is an unanswered question in the field of strongly correlated electron materials. Although it has been studied for several decades, there is still no consensus about how this new phase forms. Understanding the hidden order phase formation is not only an intellectual problem, it will also advance concepts for designing quantum materials with new exotic properties. Many hidden order scenarios are based on the assumption of certain ground-state symmetries and the present study addresses this aspect. A spectroscopic technique, nonresonant inelastic X-ray scattering, that has become available through the use of high-brilliance synchrotrons, allows us to measure directly in a bulk-sensitive experiment the symmetry of the 5*f* ground-state wave function in URu_2Si_2.

Author contributions: L.H.T. and A.S. designed research; M.S., S.A., A.A.-Z., M.M.S., L.H.T., and A.S. performed research; Y.H., M.G., and A.d.V. contributed new reagents; M.W.H. provided the code for data analysis; M.S. and M.W.H. analyzed data; and M.S., P.T., L.H.T., and A.S. wrote the paper.

The authors declare no conflict of interest.

This article is a PNAS Direct Submission.

Freely available online through the PNAS open access option.

[1]Present address: Institute for Theoretical Physics, Heidelberg University, 69120 Heidelberg, Germany.

[2]Present address: Physics Department, Faculty of Science, Beirut Arab University, Beirut 11072809, Lebanon.

[3]To whom correspondence should be addressed. Email: severing@ph2.uni-koeln.de.

This article contains supporting information online at www.pnas.org/lookup/suppl/doi:10.1073/pnas.1612791113/-/DCSupplemental.

PHYSICS

$$\Gamma_1^{(1)}(\theta) = \cos(\theta)\,|0\rangle + \sin(\theta)\sqrt{\frac{1}{2}}(|4\rangle + |-4\rangle)$$

$$\Gamma_1^{(2)}(\theta) = \sin(\theta)\,|0\rangle - \cos(\theta)\sqrt{\frac{1}{2}}(|4\rangle + |-4\rangle)$$

$$\Gamma_2 = \sqrt{\frac{1}{2}}(|4\rangle - |-4\rangle)$$

$$\Gamma_3 = \sqrt{\frac{1}{2}}(|2\rangle + |-2\rangle)$$

$$\Gamma_4 = \sqrt{\frac{1}{2}}(|2\rangle - |-2\rangle)$$

$$\Gamma_5^{(1)}(\phi) = \cos(\phi)\,|\mp 1\rangle + \sin(\phi)\,|\pm 3\rangle$$

$$\Gamma_5^{(2)}(\phi) = \sin(\phi)\,|\mp 1\rangle - \cos(\phi)\,|\pm 3\rangle$$

Here, the values θ and ϕ define the mixing of states that have equal irreducible representation, that is, the singlet states $\Gamma_1^{(1,2)}$ and doublet states $\Gamma_5^{(1,2)}$. The phase relations between the J_z states are defined such that the operator $\hat{J}_x$ is nonnegative. Note that $\Gamma_1^{(1)}(90°) = -\Gamma_1^{(2)}(0°)$ and $\Gamma_5^{(2)}(90°) = \Gamma_5^{(1)}(0°)$ and, depending on the mixing angles ϕ and θ, the CEF states correspond to pure J_z states ($\Gamma_1^{(1)}(90°) \Leftrightarrow |4\rangle + |-4\rangle$, $\Gamma_2 \Leftrightarrow |4\rangle - |-4\rangle$, $\Gamma_1^{(2)}(90°) \Leftrightarrow |0\rangle$, $\Gamma_5^{(1)}(90°) \Leftrightarrow |\pm 3\rangle$, and $\Gamma_5^{(2)}(90°) \Leftrightarrow |\pm 1\rangle$).

Determining CEF excitations and their symmetry in intermetallic U compounds is by no means trivial because the $5f$ electrons are more itinerant than, for example, the $4f$ electrons in the rare earth series, and the classic tool—inelastic neutron scattering—fails to observe sharp CEF excitations (30) due to dispersive effects and the large intrinsic widths that goes along with itinerant states. Nevertheless, there have been many experimental and also theoretical attempts to determine the symmetries of the $5f$ ground state and low-lying electronic states in URu_2Si_2, and in literature, a wide spectrum of different scenarios can be found. The anisotropy of the static susceptibility is well described with a $\Gamma_1^{(1)}$ singlet ground state, a Γ_2 as a first excited state and the next states above 15 meV [170 K] (31). Analyses of elastic constant measurements find similar results (32). Also Kiss and Fazekas (33), Hanzawa (34), and Kusunose et al. (35) favor a $\Gamma_1^{(1)}$, the model of Kiss and Fazekas being also compatible with a $\Gamma_1^{(2)}$ singlet ground state (33), but these authors all propose different first excited states from their theoretical considerations. Haule and Kotliar (29) also propose two low-lying singlet states, a Γ_2 singlet ground state and a $\Gamma_1^{(2)}$ as a first excited state, a scenario that is compatible with the interpretation of polarized Raman studies that find a resonance at 1.6 meV in the A_{2g} channel in the *HO* phase (18, 19)*. Thermodynamic measurements by Santini and Amoretti (36) and resonant X-ray scattering data by Nagao and Igarashi (37) are interpreted in terms of a Γ_3-singlet ground state with the $\Gamma_1^{(1)}$ as a first excited state or alternatively with a $\Gamma_5^{(1)}$ ground state (37). Another elastic constant study by Kuwahara et al. (38) yields a Γ_4 as a lowest state. $\Gamma_5^{(1)}$, and $\Gamma_5^{(2)}$ doublets as ground states are concluded by thermodynamic studies of diluted URu_2Si_2 (39 and theoretical considerations by Ohkawa and Shimizu (40) and Chandra et al. (41). Finally O-edge X-ray absorption measurements by Wray et al. (42) favor the $\Gamma_5^{(1)}$ and Sugiyama et al. the $\Gamma_5^{(2)}$ doublet (43) as ground state.

There is clearly room for clarification. Hence, we aim at determining the symmetries of the ground state and low-lying states in URu_2Si_2 using a spectroscopic method that directly probes the U $5f$ shell. We performed a core-level NIXS at the U $O_{4,5}$-edges ($5d \rightarrow 5f$) with hard X-rays (≈10 keV) and large momentum transfers ($|\mathbf{q}| \approx 9.6$ Å^{-1}). NIXS is a photon-in-photon-out technique that was used in the recent past on single crystals for determining the wave functions of cerium based systems (44, 45). In NIXS, the direction dependence of the momentum transfer $\vec{q}$ is used in analogy to the linear polarization dependence in an X-ray absorption spectroscopy (XAS) experiment (e.g., ref. 46 and also ref. 42) and accordingly "multipole selection rules" give access to the ground state symmetry (dipole for XAS). The higher multipoles that contribute significantly to the scattering function $S(\vec{q},\omega)$ at large momentum transfers contain more information than dipole so that, e.g., asymmetries with higher than twofold rotational symmetry can be detected (44, 47). In addition, at the U $O_{4,5}$-edge these excitations are significantly narrower than the dipole signal, which is strongly broadened due to the proximity of continuum states (48). Most importantly, it should be mentioned that a NIXS experiment does not involve an intermediate state so that the quantitative modeling is as straightforward as for XAS and the use of hard X-rays makes the signal truly bulk-sensitive in contrast to a soft XAS or soft resonant inelastic X-ray scattering (RIXS) experiment.

Results

Several NIXS studies, also on uranium compounds, show experimentally and theoretically how the multiplet excitations develop with increasing momentum transfer (44, 48–51). However, for convenience of the reader, we recapitulate briefly the principle of NIXS: when working at large-momentum transfers, the expansion of the transition operator $\exp(i\vec{q}\vec{r})$ in spherical harmonics cannot be truncated after the first term, thus giving rise to excitations due to quadru-, octupole, and higher-order contribution in $S(\vec{q},\omega)$. Fig. 1 shows the three nonvanishing contributions to $S(\vec{q},\omega)$ calculated for the U $O_{4,5}$-edge; the radial part as function of momentum transfer in Fig. 1*A* and the isotropic spectra in Fig. 1*B*, each for the dipole and higher-multipole contributions. The excitations due to scattering from higher multipoles contribute substantially to the total intensity already for momentum transfers of $|\mathbf{q}| \approx 9.6$ Å^{-1}. Performing such an experiment on a single crystal and measuring the q-direction dependence will give $S(\vec{q},\omega)$. This measurement then can be used for the CEF analysis where each state will have a specific direction dependence.

Fig. 2*A* shows the simulation of $S(\vec{q},\omega)$ of the $5d \rightarrow 5f$ transition ($O_{4,5}$-edge) for the nine states of the $J = 4$ ground state multiplet, i.e., the f^2 configuration. Contributions from other valence configurations are neglected. For more detailed

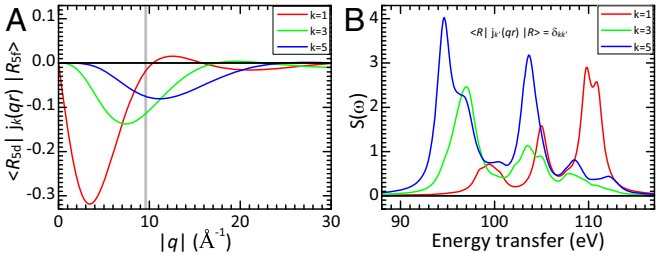

Fig. 1. Momentum $|\vec{q}|$ dependence (*A*) and energy dependence (*B*) of the scattering function $S(\vec{q},\omega)$ at the U $O_{4,5}$-edge ($5d^{10}4f^2 \rightarrow 5d^9 4f^3$) for dipole ($k = 1$), octupole ($k = 3$), and dotriacontapole ($k = 5$) scattering orders. The gray vertical line marks the $|q|$-range of the experiment. Note: features above ≈106 eV appear unrealistically narrow because the proximity of continuum states is not accounted for.

* Note, not only $\Gamma_1 \rightleftharpoons \Gamma_2$ but also $\Gamma_3 \rightleftharpoons \Gamma_4$ and $\Gamma_5 \rightleftharpoons \Gamma_5$ are Raman-active in the A_{2g} channel [Buhot et al. (supplemental material in ref. 18)].

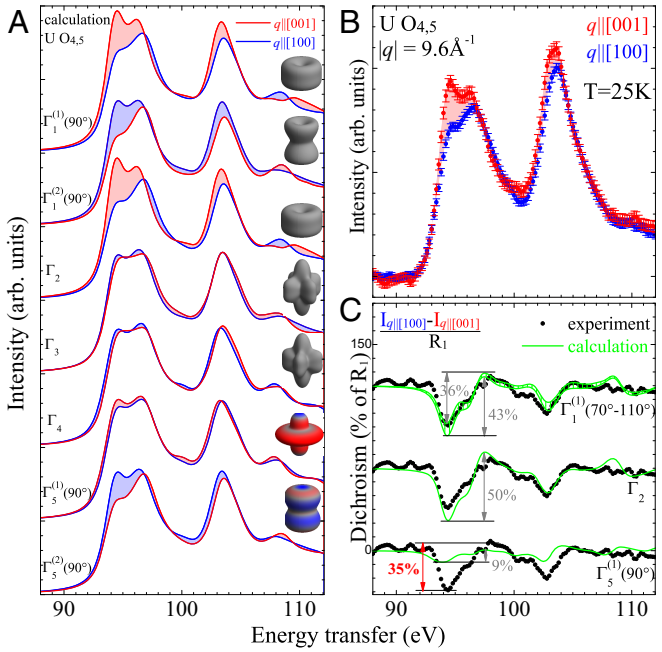

Fig. 2. (*A–C*) NIXS measurements of the U $O_{4,5}$-edge for $|\mathbf{q}| = 9.6$ Å^{-1} and corresponding calculations for $5d^{10}4f^2 \rightarrow 5d^9 4f^3$. (*A*) Simulation of $S(\vec{q},\omega)$ of U crystal-field states for $J = 4$ in D_{4h} symmetry for the two directions $\hat{q}_{||}[100]$ (blue) and [001] (red). *Insets* show the corresponding electron densities (*Materials and Methods*). (*B*) NIXS data for momentum transfers $\hat{q}_{||}[100]$ (blue) and [001] (red) at T = 25 K. (*C*) Dichroism at 25 K in percentage defined as difference $I_{\hat{q}_{||}[100]} - I_{\hat{q}_{||}[001]}$ relative to peak height R_1 as defined in the isotropic data (Fig. 3), data (black dots) and calculations (green lines) for the crystal-field states with the correct sign of dichroism. Here the data points have been convoluted with a Gaussian of 0.5-eV FWHM.

information about the simulation, we refer to *Materials and Methods*. The spectra corresponding to the respective CEF states are calculated for the two directions $\hat{q}_{||}[100]$ and $\hat{q}_{||}[001]$, and some of the states exhibit a strong direction dependence. Here, θ and ϕ are chosen such that the anisotropies are maximum, i.e., for the extreme cases of pure J_z states (see definition of CEF states). The insets in Fig. 2*A* show the respective two electron $5f$ charge densities. The charge densities of the pure states in Fig. 2*A* that appear rotational invariant do show lobes for θ and $\phi \neq 0$ or 90° (Figs. S1 and S2).

The NIXS experiment was performed at large momentum transfers (*Materials and Methods, Experimental Setup*) so that the signal is dominated by higher-order scattering (beyond dipole). Data were taken below and above the *HO* transition at 5 K and 25 K and with successively rising temperature up to 300 K. All data shown are background corrected.

Before discussing the direction dependence, we first show in Fig. 3 the isotropic data (see *Materials and Methods* for construction of isotropic spectra), together with a simulation using the ionic $5f^2$ configuration for the U. We can clearly observe a very good agreement, thereby establishing that the spectrum is dominated by the atomic multiplet structure. This observation is important because it validates a posteriori the use of local probes (such as core level NIXS) to test models using also local irreducible representations. Perhaps more surprising is that a single ionic configuration can reproduce the spectrum so well despite the known covalency of the U. However, it has been explained by, for example, Gunnarson and Schönhammer (52) as well as de Groot (53), that $d \rightarrow f$ and $p \rightarrow d$ core-level XAS (NIXS) for $4f/5f$ and $3d$ compounds, respectively, highlights the spectral weight of the energetically lowest-lying (and major) configuration at the expense of those of the higher-lying configurations, making the technique extremely powerful for determining the symmetry of the ground state (*Materials and Methods, Spectroscopy*).

We now discuss the direction dependence of the data measured above the *HO* transition because they are not affected by any possible impact of the *HO*. In Fig. 2*B*, the NIXS data of URu_2Si_2 at 25 K are shown for the in-plane direction $\hat{q}_{||}[100]$ (blue dots) and out-of-plane direction $\hat{q}_{||}[001]$ (red dots). The error bars reflect the statistical error. There is a large anisotropy that can be directly compared with our simulations.

A more detailed comparison of data and simulations excludes immediately the $\Gamma_1^{(1,2)}(\theta)$ states with strong $J_z = |0\rangle$ contributions, the Γ_3 and Γ_4 singlets with $J_z = |2\rangle$ and $J_z = |-2\rangle$, as well as the $\Gamma_5^{(1,2)}(\phi)$ states with strong $J_z = |\pm 1\rangle$ weight. Actually, only singlet states with majority $|+4\rangle$ and $|-4\rangle$ or a doublet with majority $|\pm 3\rangle$ show the correct direction dependence, i.e., red over blue (Fig. 2*A*). To be more quantitative, we compare the measured dichroism of about 35% (Fig. 2*C*) with the simulated dichroism of the URu_2Si_2 wave functions in question. Here, the dichroism is defined as the difference of the intensities for $\hat{q}_{||}[100]$ and $\hat{q}_{||}[001]$ relative to the peak height R_1 of the isotropic spectrum (Fig. 3). We find that $\Gamma_1^{(1)}(90°)$ [or $\Gamma_1^{(2)}(0°)$] and also Γ_2 reproduce the size of the anisotropy quite well, although their dichroism is with 43 or 50% slightly larger than the measured value. A $\Gamma_1^{(1)}$ state of majority $J_z = |4\rangle$ and $|-4\rangle$ symmetry, but with some $J_z = |0\rangle$ [$\Gamma_1^{(1)}(70°$ or $110°)$] would produce a slightly smaller dichroism of about 36% (Fig. 2*C*).

The $\Gamma_5^{(1)}(90°)$ [or $\Gamma_5^{(2)}(0°)$], i.e., the doublet states with the highest amount of $J_z = |\pm 3\rangle$, do not yield sufficient dichroism: the dichroism of 9% is by a factor of 4 too small and would decrease further or even change sign with increasing amount of $|\pm 1\rangle$. [In the following, we skip writing out the $\Gamma_i^{(2)}$ alternative state because of $\Gamma_i^{(1)}(90°) = -\Gamma_i^{(2)}(0°)$, $i = 1$ or 5.]

Fig. 4*A* shows the ac asymmetry of the scattering function for all temperatures. Also, here, the error bars reflect the statistical error. We find that within the error bars the 5 K and 25 K are identical. We further find that there is no change with temper-

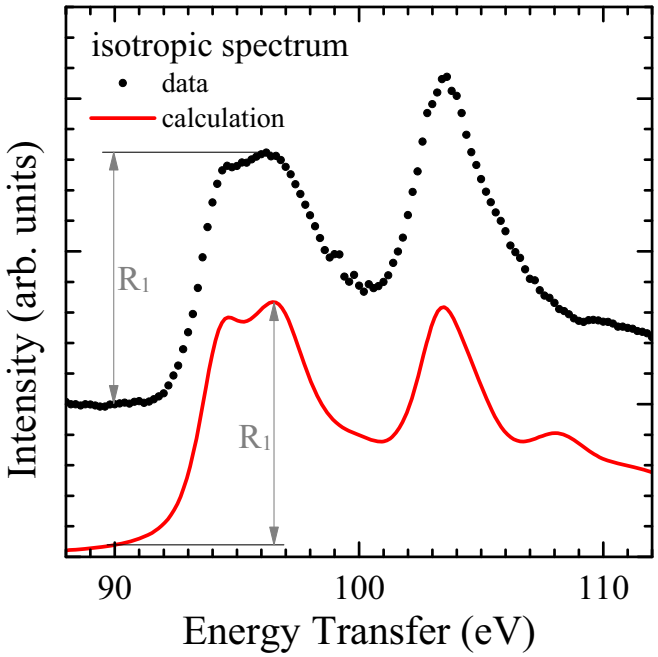

Fig. 3. Experimental (black dots) and simulated (red line) isotropic spectrum of URu_2Si_2 at the U $O_{4,5}$-edge ($5d^{10}4f^2 \rightarrow 5d^9 4f^3$) for T $\leq$ 25 K. For details, see *Materials and Methods, Isotropic Spectrum*.

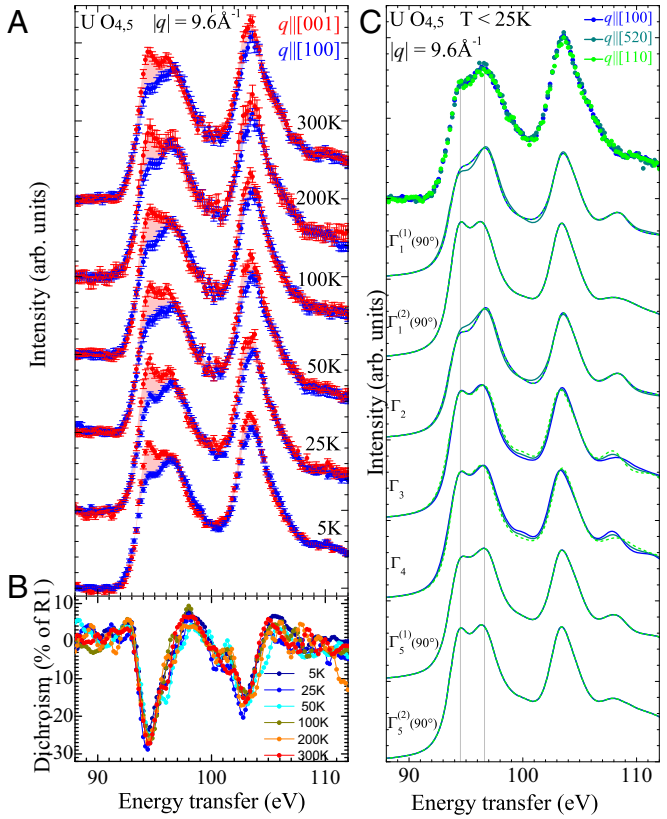

Fig. 4. (*A*) Temperature dependence of the URu_2Si_2 U $O_{4,5}$-edge NIXS spectra for $\hat{q}_{\parallel}$[100] (blue dots) and $\hat{q}_{\parallel}$[001] (red dots). For better comparison, the *T* dependent data are underlain with the difference in spectral weight of the 5 K data. (*B*) Dichroism $I_{\hat{q}_{\parallel}[100]}$-$I_{\hat{q}_{\parallel}[001]}$ for all temperatures, convoluted with a Gaussian of 0.5-eV FWHM. (*C*) NIXS data and simulations ($5d^{10}4f^2 \rightarrow 5d^9 4f^3$) for in-plane momenta $\hat{q}$ parallel to [100] and for $\hat{q}$ turned toward [010] by 22.5° and 45°, i.e., $\hat{q}_{\parallel}$[100] (blue), $\hat{q}_{\parallel}$[520] (dark green), and $\hat{q}_{\parallel}$[110] (light green) for all CEF states.

ature up to 300 K as is demonstrated by plotting the dichroism for all temperatures in Fig. 4*B*. The Boltzmann population with temperature of any state other than the $\Gamma_1^{(1)}(70°–90°–110°)$, and Γ_2 state will change the direction dependence of the scattering (compare Fig. 2*A*). Hence, we conclude from the absence of any changes in the spectra up to 300 K that the ground state consists mainly of the $\Gamma_1^{(1)}(70°–90°–110°)$ or the Γ_2 singlet or that one of the two singlets forms the ground state with the respective other state close in energy. We can further estimate from the impact of thermal occupation that the states with weak dichroism like the $\Gamma_5^{(1)}(90°)$, Γ_3 and Γ_4 must be higher than 150 K (13 meV), whereas states with stronger opposite anisotropy must be even higher in energy.

Fig. 4*C* shows data taken within the plane, for $\hat{q}_{\parallel}$[100] and for two directions 22.5° and 45° toward [010], as well as the respective simulations for all CEF states. Neither below nor above the *HO* order transition can we resolve any anisotropy within the statistical error bar. This result does not contradict our previous findings that either one of the two singlet states $\Gamma_1^{(1)}(70°–90°–110°)$ and Γ_2 forms the ground state because the asymmetries expected from simulations are rather small and most likely covered by statistics of this low count experiment. The in-plane data even confirm the out-of-plane data when comparing the measured and simulated shape of the spectra: for example, the peak at 94 eV is clearly smaller than the peak at 97 eV for the simulated $\Gamma_1^{(1)}(90°)$ and Γ_2 spectra (gray lines in Fig. 4*C*), in agreement with the data, whereas the two peaks are about the same for all other states. For the in-plane simulation for different values of θ and ϕ, we refer to Fig. S2.

Discussion

Our results of a ground state that consists mainly of $\Gamma_1^{(1)}(70°–90°–110°)$ and/or Γ_2 agree well with the description of the anisotropy of the static susceptibility (31) and the analysis of the temperature dependence of the elastic constants (32), which are well described with a $\Gamma_1^{(1)}$ of majority $J_z = +4$ and -4, a Γ_2 as a first excited state, and another state above 150 K. Our results also confirm DMFT calculations that finds these two singlet states as low-lying states close in energy [ref. 29 and supplementary materials in Kung et al. (19)], but the experiment yields the additional information that the $J_z = +4$ and -4 in the Γ_1 is dominating. We further would like to stress that linear polarized XAS data at the U $O_{4,5}$-edge (42) also agree with our findings in the sense that both, the NIXS and XAS dichroism, rule out the $\Gamma_1^{(2)}(90°)$ [or $\Gamma_1^{(1)}(0°)$], the Γ_3, or the Γ_4 as possible ground states and find no temperature dependence across the *HO* transition. The smaller direction dependence that lets the authors of ref. 42 assign the $\Gamma_5^{(1)}$ doublet as ground state might be due to the higher surface sensitivity of the XAS experiment.

A pure $\Gamma_1^{(1)}(70°–90°–110°)$ or Γ_2 or both close in energy does confront us with the dilemma that neither would break the C_4 in-plane symmetry, as suggested by the torque (21), high precision X-ray (22), and elastoresistance (23) results nor would an ordering out of a singlet state yield sufficient loss of entropy across the *HO* transition. To allow for a rank-5 E^- *HO* parameter, as in the fully microscopic itinerant approach (54, 55), the inclusion of the twofold degenerate CEF state of E-type is a necessity in the present more localized picture. Also, the interpretation of the resonance intensity in the main A_{2g} and other Raman channels in terms of a staggered chirality density wave requires a mixing of Γ_1 and Γ_2 singlet states that support a hexadecapole-type hidden order parameter. The model of Kung et al. (19) contains both dominant A_{2g} and subdominant B_{1g} symmetry parts. The latter involves higher energy CEF states and coupling to the lattice leads to a secondary orthorhombic distortion that leaves only twofold symmetry. As a result, resonance intensity leaks into forbidden channels.

Our experiment shows that the CEF components are mainly of the $\Gamma_1^{(1)}(90°)$ or Γ_2 singlet type, but we did not observe the theoretically maximum possible dichroism (Fig. 2*C*), so that the data allow the presence of some other symmetry. The mixing of an irreducible representation, other than $\Gamma_1^{(1)}(70°–90°–110°)$ or Γ_2, into the ground state cannot rely on Boltzmann occupation because that would have been observable in the temperature dependence of the NIXS data. However, a Kondo-type mechanism where an f^3 Kramers doublet hybridizes with the CEF manifold of the energetically more favorable $f^2\epsilon_k^{+1}$ configuration is feasible for constructing a ground state with different f^2 CEF characters. Here, ϵ_k^{+1} denotes an electron in the host conduction band. We recall that a hybridization gap of 13 meV opens up below 27 K (13), which is also seen in the DMFT calculation that includes these Kondo processes (19, 29). The stabilization energy of this Kondoesque wave function should be of the same order as the hybridization gap and the contributing CEF configurations should also be within this energy range.

Summary

The bulk-sensitive, U $O_{4,5}$ NIXS data of URu_2Si_2 exhibit the atomic multiplet structure of the f^2 configuration. The huge out-of-plane anisotropy shows that the symmetry of the ground state consists mainly of the $\Gamma_1^{(1)}(90°)$ or Γ_2 singlet states in the U^{4+} (f^2) configuration and/or that these two states are close in

energy. The data do not exhibit any temperature dependence, neither across the HO phase transition nor in the temperature interval up to 300 K, the latter setting constraints to the proximity of next-higher excited states. Scenarios for constructing a ground state that is a superposition of different irreducible representations without relying on Boltzmann statistics are discussed.

Materials and Methods

Samples. A high-quality single crystal of URu_2Si_2 was grown with the traveling zone method in the two-mirror furnace in Amsterdam under high-purity (6N) argon atmosphere. The crystal was checked and oriented with X-ray Laue diffraction for its single-crystalline nature. The oriented crystal was cut using the spark-erosion method, after which the relevant surfaces [(100), (110), and (001)] were polished. A bar-shaped piece of the single crystal was characterized by resistance measurements.

Experimental Setup. The scattering function $S(\vec{q},\omega)$ was measured in a NIXS experiment at the beamline ID20 at European Synchrotron Radiation Facility (ESRF). Two monochromators [Si(111) and Si (311)] set the incident energy to 9,690 eV, and the scattered intensity was analyzed by one column of three Si(660) crystal analyzers at an in-plane scattering angle of $2\vartheta = 153^\circ$ and detected in a Maxipix 2D detector with an overall energy resolution of about 0.8 eV. This setting corresponds to a momentum transfer of $|\mathbf{q}| = 9.6$ Å^{-1}. The crystals with (100), (110), and (001) surfaces allowed realizing $\hat{q}_{||}$[100], [110], and [001] in specular geometry and also other directions when going off specular. It turned out that specular geometry (same path for photon in as for photon out) is not necessary because $\hat{q}_{||}$[110] measured specular on the (110) crystal and 45° off specular on the (100) crystal gave the same result. For cooling, the samples were mounted in a He flow cryostat. The elastic line was measured before each setting to determine the zero energy transfer and exact instrumental resolution for each analyzer. The spectra of the U $O_{4,5}$-edges were then normalized to their pre-edge intensity. Scans over a wide energy range were taken to correct for the Compton scattering and some minor constant background. The Compton background was fitted to a Gaussian and then subtracted from the data.

Spectroscopy. Why does *O*-edge XAS or NIXS resemble the f^2 multiplet structure and why is *O*-edge XAS or NIXS sensitive to the symmetry? The energy order of the local configurations of the ground state and of the NIXS/XAS core-hole final state problem is identical, so that the spectral weights of the other local configurations are strongly suppressed due to quantum mechanical interference effects. These interrelations are well explained, for example, by Gunnarsson and Schönhammer (figure 7 in ref. 52) for the case of Ce $M_{4,5}$ XAS and by de Groot (53) for the case of 3*d* transition metal $L_{2,3}$ XAS. A quote from the latter is as follows: "XPS is sensitive to the charge transfer effects...while XAS is sensitive to the symmetry of the ground state with its characteristic multiplet" (ref. 53, pp. 549 and 550). It is important that the relevant intra- and intershell Coulomb interactions are of similar size to have the same order of configuration energies in the ground state and core-hole final state problem: this is true for the Ce $M_{4,5}$ (3*d*, 4*f*), U $O_{4,5}$ (5*d*, 5*f*), and transition metal $L_{2,3}$ (2*p*,3*d*) edges but not for the Ce $L_{2,3}$ (2*p*,5*d* with 4*f* as spectator) or U $L_{2,3}$ (2*p*,6*d* with 5*f* as spectator) because the Coulomb interaction with the 5*d* or 6*d* is negligible.

Simulations. The simulations include spin–orbit coupling and Coulomb interaction and are based on an ionic model with a U^{4+} $5f^2$ configuration. The atomic values are calculated with the Cowan code (56), but the Slater integrals for Coulomb interactions are reduced by a constant factor to account for the screening of the moments in the solid. The 5*f*–5*f* and 5*d*–5*f* reduction was adjusted to about 50% to match the experimental energy spread of the multiplet signal of the isotropic data in Fig. S1 (for construction of isotropic spectrum, see below). The ratio of multipole contributions was slightly adjusted by varying $|\mathbf{q}|$ (49). In the simulations, the actual value for $|\mathbf{q}|$ was slightly larger than according to the experimental scattering triangle because the radial part of the wave functions that enter the calculations is based on the atomic values. For all finite values of spin–orbit coupling and Coulomb interaction the $J = 4$ multiplet forms the Hund's rule ground state. The relative contributions of different angular momenta $L = 3$, 4, 5 depend on the ratio of spin–orbit coupling and Coulomb interaction and are 1, 14, and 85% for our reduction factors, respectively.

Within the $J = 4$ basis we, create the local eigenstates (Γ_1 to Γ_5) restricted to the f^2 configuration by combining different states of J_z considering the constraints by group theory. The Hamiltonian includes the local spin–orbit coupling and multipolar Coulomb interaction, which are much larger (up to 1 Rydberg) than the final-state core-hole lifetime (order of 1 eV) but neglects the effects of crystal-field, covalent bonding and band formation of the crystal, which will be smaller or of the same order of magnitude as the core-hole lifetime. The calculations are performed using the Quanty code (57). To account for instrumental resolution, lifetime effects, and interference effects with the continuum the multiplet lines are broadened with a Gaussian [full-width at half-maximum (FWHM) = 0.8 eV], a Lorentzian (FWHM = 1.3 eV), and a Mahan-type line shape (with an asymmetry factor 0.18 and an energy width of the continuum of 1,000 eV) to mimic the asymmetry due to the itinerancy.

Charge Densities. The charge densities are calculated for two electrons. The surface thus tells how much charge can be found in a specific direction. A charge density for a one-electron system would be an occupied orbital and a "sum" of different orbitals when the system can be represented by a single Slater determinant. The color is related to the spin density with up as red, down as blue, and zero as gray (Fig. 2*A*). For URu_2Si_2, $LSJJ_z$ coupling is often assumed whereby *L S J* and J_z are all good quantum numbers. Doing so results in density plots with many more features than in the present report. This assumption is basically equivalent to saying that F_2, F_4, and F_6 Slater integrals are infinitely larger than the spin–orbit coupling. That approximation is not valid, and spin–orbit coupling mixes states *LS* with states *L*+1 *S*-1 or *L*-1 *S*+1. This mixing is included in our calculations. Furthermore, we know that both the multipole part of the Coulomb interaction as well as the spin–orbit interaction are not (not really) screened in a solid. In other words, the U 5*f* shell in URu_2Si_2 is between *LS* and *jj* coupling and was taken into account.

Isotropic Spectrum. The isotropic spectrum is given by the trace of the conductivity tensor. For dipole transitions ($k = 1$), this tensor can be written as a 3×3 matrix with two independent diagonal elements in D_{4h} symmetry. However, for higher multipoles, the conductivity tensor has also a higher dimension, i.e., 7×7 for octupole ($k = 3$) and 11×11 for dotriacontapole ($k = 5$). Here, we obtain the experimental isotropic spectrum containing these three relevant conductivity tensors by combining 10 independently measured directions. The calculated isotropic spectrum is obtained by averaging over all CEF states. The red line in Fig. 3 is the simulation of the isotropic data after optimizing the respective parameters.

ACKNOWLEDGMENTS. We thank Artem Nikitin for characterizing the sample by transport. M.S. and A.S. received support from Deutsche Forschungsgemeinschaft Project SE 1441/1-2. We further acknowledge European Synchrotron Radiation Facility (ESRF) for provision of synchrotron radiation facilities (Proposals HC1533 and HC2252).

1. Santini P, et al. (2009) Multipolar interactions in *f*-electron systems: The paradigm of actinide dioxides. *Rev Mod Phys* 81(2):807–863.
2. Pfleiderer C (2009) Superconducting phases of *f*-electron compounds. *Rev Mod Phys* 81(4):1551–1624.
3. Löhneysen Hv, Rosch A, Vojta M, Wölfle P (2007) Fermi-liquid instabilities at magnetic quantum phase transitions. *Rev Mod Phys* 79(3):1015–1075.
4. Palstra TTM, et al. (1985) Superconducting and magnetic transitions in the heavy-fermion system URu_2Si_2. *Phys Rev Lett* 55(24):2727–2730.
5. Schlabitz W, et al. (1986) Superconductivity and magnetic ordering a strongly interacting fermi-system: URu_2Si_2. *Z Phys B Condens Matter* 62(2):171–177.
6. Maple MB, et al. (1986) Partially gapped fermi surface in the heavy-electron superconductor URu_2Si_2. *Phys Rev Lett* 56(2):185–188.
7. Kasahara Y, et al. (2007) Exotic superconducting properties in the electron-hole-compensated heavy-fermion semimetal URu_2Si_2. *Phys Rev Lett* 99(11): 116402.
8. Amitsuka H, et al. (2007) Pressure - temperature phase diagram of the heavy-electron superconductor URu_2Si_2. *J Magn Magn Mater* 310(2):214–220.
9. Meng JQ, et al. (2013) Imaging the three-dimensional Fermi-surface pairing near the hidden-order transition in URu_2Si_2 using angle-resolved photoemission spectroscopy. *Phys Rev Lett* 111(12):127002.
10. Bareille C, et al. (2014) Momentum-resolved hidden-order gap reveals symmetry breaking and origin of entropy loss in URu_2Si_2. *Nat Commun* 5:4326.
11. Chatterjee S, et al. (2013) Formation of the coherent heavy fermion liquid at the hidden order transition in URu_2Si_2. *Phys Rev Lett* 110(18):186401.

12. Hassinger E, et al. (2010) Similarity of the Fermi surface in the hidden order state and in the antiferromagnetic state of URu_2Si_2. *Phys Rev Lett* 105(21):216409.
13. Park WK, et al. (2012) Observation of the hybridization gap and Fano resonance in the Kondo lattice URu_2Si_2. *Phys Rev Lett* 108(24):246403.
14. Aynajian P, et al. (2010) Visualizing the formation of the Kondo lattice and the hidden order in URu_2Si_2. *Proc Natl Acad Sci USA* 107(23):10383–10388.
15. Schmidt AR, et al. (2010) Imaging the Fano lattice to hidden order transition in URu_2Si_2. *Nature* 465(7298):570–576.
16. Broholm C, et al. (1991) Magnetic excitations in the heavy-fermion superconductor URu_2Si_2. *Phys Rev B Condens Matter* 43(16):12809–12822.
17. Wiebe CR, et al. (2007) Gapped itinerant spin excitations account for missing entropy in the hidden-order state of URu_2Si_2. *Nat Phys* 3(2):96–99.
18. Buhot J, et al. (2014) Symmetry of the excitations in the hidden order state of URu_2Si_2. *Phys Rev Lett* 113(26):266405.
19. Kung HH, et al. (2015) Chirality density wave of the "hidden order" phase in URu_2Si_2. *Science* 347(6228):1339–1342.
20. Bourdarot F, et al. (2010) Precise study of the resonance at Q_0=(1,0,0) in URu_2Si_2. *J Phys Soc Jpn* 79(6):064719.
21. Okazaki R, et al. (2011) Rotational symmetry breaking in the hidden-order phase of URu_2Si_2. *Science* 331(6016):439–442.
22. Tonegawa S, et al. (2014) Direct observation of lattice symmetry breaking at the hidden-order transition in URu_2Si_2. *Nat Commun* 5:4188.
23. Riggs SC, et al. (2015) Evidence for a nematic component to the hidden-order parameter inURu_2Si_2 from differential elastoresistance measurements. *Nat Commun* 6: 6425.
24. Mydosh JA, Oppeneer PM (2011) *Colloquium*: hidden order, superconductivity, and magnetism: The unsolved case of URu_2Si_2. *Rev Mod Phys* 83(4):1301–1322.
25. Jeffries JR, Moore KT, Butch NP, Maple MB (2010) Degree of 5*f* electron localization in URu_2Si_2: electron energy-loss spectroscopy and spin-orbit sum rule analysis. *Phys Rev B* 82(3):033103.
26. Booth CH, et al. (2016) Probing 5*f*-state configurations in URu_2Si_2 with U L_{III}-edge resonant x-ray emission spectroscopy. *Phys Rev B* 94(4):045121.
27. Fujimori SI, et al. (2016) Electronic structures of uranium compounds studied by soft x-ray photoelectron spectroscopy. *J Phys Soc Jpn* 85(6):062001.
28. Zwicknagl G, Yaresko A, Fulde P (2003) Fermi surface and heavy masses for UPd_2Al_3. *Phys Rev B* 68(5):052508.
29. Haule K, Kotliar G (2009) Arrested Kondo effect and hidden order in URu_2Si_2. *Nat Phys* 5(11):796.
30. Broholm C, et al. (1987) Magnetic excitations and ordering in the heavy-electron superconductor URu_2Si_2. *Phys Rev Lett* 58(14):1467–1470.
31. Nieuwenhuys GJ (1987) Crystalline electric field effects in UPt_2Si_2 and URu_2Si_2. *Phys Rev B Condens Matter* 35(10):5260–5263.
32. Yanagisawa T, et al. (2013) Hybridization-driven orthorhombic lattice instability in URu_2Si_2. *Phys Rev B* 88(19):195150.
33. Kiss A, Fazekas P (2005) Group theory and octupolar order in URu_2Si_2. *Phys Rev B* 71(5):054415.
34. Hanzawa K (2012) Crystalline electric field effects and hidden order in URu_2Si_2. *J Phys Soc Jpn* 81(11):114713.
35. Kusunose H, Harima H (2011) On the hidden order in URu_2Si_2 antiferro hexadecapole order and its consequences. *J Phys Soc Jpn* 80(8):084702.
36. Santini P, Amoretti G (1994) Crystal field model of the magnetic properties of URu_2Si_2. *Phys Rev Lett* 73(7):1027–1030.
37. Nagao T, Igarashi JI (2005) Resonant x-ray scattering from URu_2Si_2. *J Phys Soc Jpn* 74(2):765–772.
38. Kuwahara K, et al. (1997) Lattice instability and elastic response in the heavy electron system URu_2Si_2. *J Phys Soc Jpn* 66(10):3251–3258.
39. Amitsuka H, Sakakibara T (1994) Single uranium-site properties of the dilute heavy electron system $U_xTh_{1-x}Ru_2Si_2$ ($x \leq 0.07$). *J Phys Soc Jpn* 63(2):736–747.
40. Ohkawa FJ, Shimizu H (1999) Quadrupole and dipole orders in URu_2Si_2. *J Phys Condens Matter* 11(46):L519–L524.
41. Chandra P, Coleman P, Flint R (2013) Hastatic order in the heavy-fermion compound URu_2Si_2. *Nature* 493(7434):621.
42. Wray LA, et al. (2015) Spectroscopic determination of the atomic *f*-electron symmetry underlying hidden order in URu_2Si_2. *Phys Rev Lett* 114(23):236401.
43. Sugiyama K, et al. (1999) Metamagnetic transition in a heavy fermion superconductor URu_2Si_2. *J Phys Soc Jpn* 68(10):3394–3401.
44. Willers T, et al. (2012) Determining the in-plane orientation of the ground-state orbital of $CeCu_2Si_2$. *Phys Rev Lett* 109(4):046401.
45. Sundermann M, et al. (2015) $CeRu_4Sn_6$: A strongly correlated material with nontrivial topology. *Sci Rep* 5:17937.
46. Hansmann P, et al. (2008) Determining the crystal-field ground state in rare earth heavy fermion materials using soft-x-ray absorption spectroscopy. *Phys Rev Lett* 100(6):066405.
47. Gordon RA, Haverkort MW, Sen Gupta S, Sawatzky GA (2009) Orientation-dependent x-ray Raman scattering from cubic crystals: Natural linear dichroism in MnO and CeO_2. *J Phys Conf Ser* 190(1):012047.
48. Sen Gupta S, et al. (2011) Coexistence of bound and virtual-bound states in shallow-core to valence x-ray spectroscopies. *Phys Rev B* 84(7):075134.
49. Gordon RA, et al. (2008) High multipole transitions in NIXS: Valence and hybridization in 4f systems. *Europhys Lett* 81(2):26004.
50. Bradley JA, et al. (2010) Probing electronic correlations in actinide materials using multipolar transitions. *Phys Rev B* 81(19):193104.
51. Caciuffo R, et al. (2010) Uranium 5*d* − 5*f* electric-multipole transitions probed by nonresonant inelastic x-ray scattering. *Phys Rev B* 81(19):195104.
52. Gunnarsson O, Schönhammer K (1983) Electron spectroscopies for Ce compounds in the impurity model. *Phys Rev B* 28(28):4315–4341.
53. de Groot F (1994) X-ray absorption and dichroism of transition metals and their compounds. *J Electron Spectros Relat Phenom* 67(4):529–622.
54. Ikeda H, et al. (2012) Emergent rank-5 nematic order in URu_2Si_2. *Nat Phys* 8(7):528–533.
55. Thalmeier P, Takimoto T, Ikeda H (2013) Itinerant multipolar order in URu_2Si_2 and its signature in magnetic and lattice properties. *Philos Mag* 94(32–33):3863–3876.
56. Cowan R (1981) The Theory of Atomic Structure and Spectra (University of California, Berkley, CA).
57. Haverkort MW (2016) *Quanty* for core level spectroscopy - excitons, resonances and band excitations in time and frequency domain. *J Phys Conf Ser* 712(1):012001.